Journal of Magnetism and Magnetic Materials 475 (2019) 76–82

Contents lists available at ScienceDirect

Journal of Magnetism and Magnetic Materials

journal homepage: www.elsevier.com/locate/jmmm

Renal perfusion assessment using magnetic nanoparticles with 7T dynamic susceptibility contrast MRI in rats

Yen-Ling Lin[a,b], Yu-Chun Lin[a,c], Li-Jen Wang[a,d], Sin-Ting Ngo[b,e], Yunn-Hwa Ma[e,f,*]

[a] Department of Medical Imaging and Intervention, Chang Gung Memorial Hospital, Linkou, Taiwan
[b] Graduate Institute of Biomedical Sciences, Chang Gung University, Taoyuan, Taiwan
[c] Department of Medical Imaging and Radiological Science, Chang Gung University, Taoyuan, Taiwan
[d] College of Medicine, Chang Gung University, Taoyuan, Taiwan
[e] Department of Physiology and Pharmacology, Chang Gung University, Taoyuan, Taiwan
[f] Department of Neurology, Chang Gung Memorial Hospital, Taoyuan, Taiwan

ARTICLE INFO

Keywords:
Magnetic nanoparticles
Magnetic resonance imaging
Dynamic susceptibility contrast
Perfusion MRI
Polyethylene glycol

ABSTRACT

Magnetic nanoparticles (MNPs) can be used as magnetic resonance imaging (MRI) contrast agent with dynamic susceptibility contrast (DSC) MRI, which is an important *in vivo* method to assess organ perfusion with multiple clinical applications. Since variations in particle size and PEGylation of MNPs may potentially influence particle-tissue interactions in the microcirculation, we evaluate their effects on rat kidneys with DSC MRI. Anesthetized Sprague Dawley rats were cannulated for intravenous injection of dextran-coated MNPs (50 nm and 250 nm; 5 mg/kg) with or without PEGylation during acquirement of DSC MRI images. The results demonstrate that both particle size and PEGylation may alter perfusion parameters. Relative mean transit time (rMTT) of 50 nm particles is 1.8 fold of that of 250 nm particles with or without PEGylation. In MNPs of 50 nm, PEGylation is associated with 38% and 25% shorter time-to-peak (TTP) and time from onset to 50% drop from peak (T50), respectively; however, PEGylation exerts no effect on these parameters of 250 nm particles. Nevertheless, particle size or PEGylation exert no influence on the prediction of relative blood flow or relative blood volume of the kidney. In conclusion, DSC MRI is a feasible method to evaluate renal perfusion and properties of MNPs in circulation.

1. Introduction

Magnetic nanoparticles (MNPs) serve an important role in a wide spectrum of biomedical applications in the recent two decades. Research interests have grown rapidly with more than two-thousands publications per year in the recent five years in the PubMed database, varying from diagnostics to therapeutics, from preclinical studies to clinical trials. Due to the biocompatibility, small size, engineerable and magnetic properties of MNPs, they can be potentially used in the biomedical fields such as magnetic separation, biosensors, tissue engineering, cell targeting and tracking, molecular and cellular imaging, targeted drug delivery, magnetic hyperthermia, and magnetic resonance imaging (MRI) contrast agent [1–4].

For diagnostics, MNPs can passively accumulate in diseased tissues *via* enhanced permeability and retention effects. Active cell targeting can be achieved by MNPs decorated with variable molecules or incorporated into liposomes with specific ligands [5]. After binding to the target cell surface markers, MNPs accumulate around the cells and may enter the cells *via* receptor-mediated internalization, resulting in enough signal alterations that can be detected by MRI. Previous studies have shown values of MNPs in the molecular diagnosis of MRI, for *in vivo* visualization of inflammation [6], tumor angiogenesis [7], and cancer cells with overexpressed tumor-associated antigens [8–11]. For therapeutics, MNPs can be designed as magnetic carriers, delivering drugs or therapeutic agents specifically into the target cells and decreasing systemic side effects [12,13]. For instance, delivery of cytotoxic drugs or therapeutic genes into cancer cells have demonstrated decreased tumor proliferation and increased apoptosis [14–16]. Furthermore, MNPs at target site can be heated up *via* alternating magnetic field to achieve magnetic hyperthermia, i.e., elevation of local temperature to 40–45 °C lasting for 30–60 min. Magnetic hyperthermia can cause cancer cell death, showing synergistic effect with radiotherapy and chemotherapy in clinical trials, reporting complete response or local control rates as 55–82% and an overall improved progression-free survival time for a varieties of tumors [4].

Many of the biomedical applications of MNPs take advantage of the

* Corresponding author at: Department of Physiology and Pharmacology, Chang Gung University, 259 Wen-Hua 1st Road, Kwei-Shan, Tao-Yuan 333, Taiwan.
E-mail address: yhma@mail.cgu.edu.tw (Y.-H. Ma).

https://doi.org/10.1016/j.jmmm.2018.11.041
Received 24 June 2018; Received in revised form 6 November 2018; Accepted 6 November 2018
Available online 13 November 2018
0304-8853/

properties of MNPs as MRI contrast agent. Owing to magnetic susceptibility, MNPs can increase the transverse relaxation rate of the surrounding water proton spins, resulting in signal drop as they pass through the vessels and tissues [17–19]. Polyethylene glycol (PEG) coating (PEGylation) of MNPs allows good biocompatibility [20,21], decreasing protein opsonization, and evading them from the capture of immunocytes in the reticuloendothelial system (RES) [22], thereby may alter the behaviors and biodistribution of MNPs in organ microenvironments [23,24].

Perfusion of an organ system is the evaluation of blood flow through the specific tissue mass of an organ system, representing the vascular microstructure of the respective organ system. Perfusion status is of vital importance for the evaluation of organ function in both physiological and pathological aspects. Different organs present different perfusion profiles owing to variable tissue histology. Clinically, MR perfusion study allows a non-invasive method for *in vivo* assessment of hemodynamic parameters [25], and has been used to evaluate the severity of renal arterial stenosis, acute rejection of transplant kidney, renal tumor differentiation and grading, and evaluation of tumor angiogenesis and therapeutic effects of anti-angiogenic agents [26–32].

There is important role for MNPs in the clinical settings of variable renal pathologies. Perfusion deficiency of kidneys may cause ischemia or infarction and resulting in renal function insufficiency. In patients with renal insufficiency such as acute kidney injury (AKI) or chronic kidney disease (CKD), the renal function has been impaired, however, traditional iodine contrast medium for computer tomography or angiography may cause further contrast-induced nephropathy under preexisting renal insufficiency [33], while gadolinium chelates for MRI may induce nephrogenic systemic fibrosis, which is likely to be an irreversible condition [34]. Moreover, in renal transplant patients, acute thrombosis of renal artery of the transplant kidney is a medical emergency and an urgent diagnosis is indicated. Since MNPs larger than 10–15 nm are generally agreed not being excreted by glomerular filtration, and no definite evidence of entering into the urine [35], they are considered safe for these renal function impaired conditions [36–38]. Therefore, MR perfusion study with MNPs as contrast agent is ideal for diagnosis for vascular occlusion or organ hypoperfusion in the renal insufficiency patients. In addition, patients with CKD may suffer from iron deficiency and an intravenous administered MNPs could serve as iron supplement [39]. To our knowledge, evaluation of renal MR perfusion parameters using MNPs in small animal was rare in the literature [40,41], and none had been done to compare the effects of different MNPs in rats.

In this study, we aim to evaluate the renal perfusion quantification with dynamic susceptibility contrast (DSC) MRI using different MNPs in rats, and we further evaluate whether variations in particle size and PEGylation of MNPs may have effects on renal microcirculation that can be observed by perfusion imaging.

2. Materials & methods

2.1. Animal preparation

The protocol was approved by the Institutional Animal Care and Use Committee of Chang Gung Memorial Hospital. Male Sprague Dawley (SD) rats (9 ~ 10 wk old; 348 ± 3 g; n = 20) from BioLASCO Taiwan Co. were anesthetized with intraperitoneal injection of Inactin® (thiobutabarbital sodium; Sigma-Aldrich, Burlingame, CA) at a dosage of 100 mg/kg. Catheterization of jugular vein with a 150 cm PE50 catheter was performed for fluid supplement with a mixture of saline and hydroxyethyl starch (Voluven®, Fresenius Kabi, Germany) solution (1:2; 30 μL/min) and administration of MNPs; cannulation of trachea and urinary bladder was conducted to ensure a patent airway and unobstructed urine flow.

2.2. MR imaging

Anesthetized SD rats were relocated into the dedicated animal 7T MRI (ClinScan 70/30, Bruker, Germany). The body temperature of each animal during the whole scan was maintained stable by circulation of heated water. The respiratory rate was monitored and gated through SA instruments software (Model 1030 Monitoring and Gating System). In addition, a Tx/Rx volume coil was exploited to acquire following images.

The MRI protocols included T2-weighted imaging, pre-contrast T2* mapping, DSC MRI, and post-contrast T2* mapping. The T2-weighted imaging was acquired using a 2D turbo spin echo sequence with repetition time (TR)/echo time (TE) = 2000/37 ms, slice thickness = 0.8 mm, field of view (FOV) = 48 × 60 mm^2, in-plane resolution = 0.313 × 0.313 mm^2, number of excitation (NEX) = 2, fat saturation and respiration gating in both coronal and transversal sections. The T2* mapping was obtained using a gradient-echo based sequence with TR = 200 ms, 5 TEs = 3.34, 9.32, 14.82, 20.32, 25.82 ms, flip angle = 40°, slice thickness = 1 mm, FOV = 50 × 60 mm^2, and NEX = 2. The DSC MRI was performed with TR/TE = 7.1/3.22 msec, flip angle = 15°, slice thickness = 0.8 mm, FOV = 48 × 60 mm^2, in-plane resolution = 0.313 × 0.313 mm^2, and 300 measurements with 1-sec temporal resolution.

The rats were given intravenous infusion of hydroxyethyl starch solution at a rate of 30 μL/min during the MRI scanning. Four groups of SD rats (5 in each group) were given intravenous injection of dextran-coated MNPs (nanomag®-D, micromod, Germany; 5 mg/kg) with particle sizes of 50 or 250 nm, either with or without PEGylation, designated as PEG(+) MNPs and PEG(−) MNPs, respectively. The MNPs were injected 20 s after the beginning of DSC MRI acquisition, lasting for 15 s, and followed by a bolus of 800 μL hydroxyethyl starch solution steadily injected for 10 s.

2.3. Image postprocessing

Image postprocessing was performed with in-house written algorithms using MATLAB (The MathWorks, Inc., Natick, Massachusetts, United States) and R software [42]. Regions of interest (ROIs) of kidneys and abdominal aorta were drawn manually. Three ROIs at anterior, posterior, and lateral portions of renal cortex and one ROI at renal medulla were chosen for each kidney, avoiding areas with obvious artifact or large vessels. One ROI was delineated in the abdominal aorta of each rat.

The signal-time curves from each ROI was visually examined. A robust local regression smoothing filter (rLowess) was applied on the signal-time curves to de-noise the data. The signal intensity was converted to tracer concentration based on the following equation, assuming a linear relationship between tracer concentration and the change in transverse relaxation rate ΔR_2 [18,36]:

$$C(t) = k \cdot \Delta R_2(t) = -\frac{k}{TE} \cdot \ln\left(\frac{S(t)}{S_0}\right) \quad (1)$$

where C(t) is the concentration of tracer varying by time, TE is the echo time, S_0 is the baseline signal, and k is a proportional coefficient that can be affected by magnetic field strength, acquisition sequence, tissue type, and properties of the contrast agent. The arterial input function (AIF) is the concentration-time curve of the input large artery of kidney. In this study, AIF was derived from abdominal aorta, since the caliber of rat renal artery was too small for precise ROI circumscription and may result in partial volume effect.

The renal impulse response function (IRF) was derived from deconvolution of concentration-time curve from AIF according to tracer-kinetic theory [43–45]. IRFs were averaged over all the cortical ROIs of the same kidney. Characteristics of the renal IRFs were described by parameters as follows: the time from onset of the upslope to peak value

(i.e. time-to-peak, TTP), time from onset to 25% drop from peak on the downslope (T25), and time from onset to 50% drop from peak on the downslope (T50). The hemodynamic parameters, the relative renal blood flow (rRBF) and relative renal blood volume (rRBV), were obtained from the height and the time integral of the IRF, respectively [43,45–47]. The relative mean transit time (rMTT) was obtained from dividing rRBV by rRBF according to the central volume theorem: rMTT = rRBV/rRBF [48].

To assess the imaging quality of the DSC MRI images, signal-to-noise ratio (SNR) were measured *via* single acquisition method [49,50]. Two ROIs each with 20 pixels were set on renal cortex and background air of the same image. SNR was defined as the quotient of mean signal intensity of renal cortex ROI to standard deviation of signal intensity of background air ROI. Six images (the 3rd, 40th, 65th, 120th, 160th, 250th images) of each rat were measured, yielding a total 120 sets of ROIs. The means and standard deviations of SNRs were calculated.

2.4. Statistical analysis

Two-way analysis of variance (ANOVA) was conducted to test for the influences of the two factors (particle size, PEGylation of MNPs) on the perfusion parameters. Post-hoc comparisons (Duncan's new multiple range test) were then used when analysis of variance was significant. Values were presented as mean ± standard error of mean (SEM). Statistical analysis was performed with R software. *P*-values < 0.05 were considered statistically significant.

2.5. Surgical intervention and histology

Approximately 1.5 h after MNP administration, the whole body perfusion was conducted from the left ventricle of the heart with a cut at the right atria using 30 ml saline, followed by 10% formalin (Buffered Formalde-Fresh, Fisher Scientific, Fair Lawn, NJ). The lung, liver, and kidney of the rats were then surgically excised, immediately fixated in formalin for 24 h prior to paraffin-embedding. The sections of the organs were stained with Prussian blue with nuclear fast red as counterstain at the Department of Pathology, Chang Gung Memorial Hospital.

3. Results

3.1. DSC perfusion MRI

After bolus injection of MNPs, DSC MRI images show dynamic change in signal intensity with 1-second temporal resolution. Representative ROIs are shown in Fig. 1A. A sudden drop in signal intensity is observed first in abdominal aorta, then in renal cortex and medulla, and finally in the inferior vena cava (Fig. 1B). The signal-time curves (STCs) obtained from ROIs demonstrate an initial abrupt drop in signal intensity followed by a gradual recover, but not returning to the baseline signal (Fig. 2A), which is compatible with the first-pass of MNP bolus through the kidneys and followed by particle recirculation. The concentration-time curves (CTCs) converted from STCs according to Eq. (1) are illustrated in Fig. 2B.

The tissue impulse response functions (IRFs) of kidneys after injection of four groups of MNPs are demonstrated in Fig. 3. There was no significant difference in IRFs of the bilateral kidneys of the same rat, then the IRFs of the same anatomical location (renal cortex, renal medulla) were averaged between both kidneys for quantitative analysis. No significant difference was observed in the IRFs obtained from renal cortex *vs.* medulla of the same kidney. ANOVA was conducted with the cortical data for its relevance to the renal function.

The signal-to-noise ratios (SNRs) of DSC MRI images in acquisition of 250 nm particles are 10.0 ± 0.9 and 10.2 ± 1.5 for PEG(+) and PEG(−) MNPs, respectively. The SNRs in acquisition of 50 nm particles are 9.8 ± 0.9 and 10.1 ± 1.1 for PEG(+) and PEG(−) MNPs, respectively. Overall, the SNR is 10.0 ± 1.1 (n = 20) in the acquisition.

3.2. Influences of particle size and PEGylation on the perfusion parameters

The results of descriptive statistics and two-way ANOVA for the perfusion parameters are summarized in Fig. 4. Overall, particle size is a main effect for the perfusion parameters TTP, T25, T50, and rMTT, with 50 nm particles presenting significantly longer time intervals. PEGylation is a main effect for T50 ($p < 0.01$), rMTT ($p < 0.01$), with PEG(+) MNPs showing shorter time intervals. However, the main effects of TTP and T50 are recognized under interactions between particle size and PEGylation.

The interactions between particle size and PEGylation are significant for TTP ($p < 0.01$) and T50 ($p < 0.05$), i.e., the effects of PEGylation for TTP and T50 depend on particle size. Specifically, PEGylation associates with shortening of TTP and T50 for the 50 nm particles, but no significant effect for the 250 nm particles.

Post hoc analysis further reveals that PEGylation is associated with shorter TTP, T50, and rMTT, and is significant only for the 50 nm particles. On the contrary, the effect of PEGylation is not statistically significant for the 250 nm particles. Neither particle size, PEGylation, or their interaction shows significant effect on rRBF and rRBV. Shapiro-Wilk tests and Levene's tests are conducted for normality and homogeneity checks and the assumptions are met ($p > 0.05$; Figs. S1–3).

3.3. Histology

Microscopic examination of Prussian blue-stained histological sections shows no evidence of MNPs retention in the sections of lungs or kidneys (Fig. 5). In contrast, the MNPs are detected in all the liver sections as blue pigment.

4. Discussion

Our study demonstrates that particle size of MNPs is an important main factor to influence the perfusion parameters. Large-sized MNPs present with steeper slopes of wash in and washout, and faster mean transit time through the kidneys. Small-sized MNPs show slower wash in, delayed washout, and overall larger mean transit time.

One possible explanation for the more concentrated behavior of large MNPs as they traverse through the kidneys is as a form of aggregates or agglomerates while they pass through the renal microcirculation. Small-sized nanoparticles may disperse in the circulation more easily, or get trapped momentarily in the renal glomerular basement membrane [51], thus elongating the overall traversing time. However, histological examination of the renal specimens showed no evidence of MNP retention or entrapment in the kidneys.

Another potential explanation for the size effect is the capture of MNPs from the RES varies according to their hydrodynamic diameters. Nanoparticles larger than 100–200 nm are cleared rapidly from the bloodstream by Kupffer cells and macrophages in liver and spleen respectively, while small particles less than 100 nm may evade from the initial hepatic and splenic clearance, being able to enter the tissue macrophages, lymphatic system, and regional lymph nodes [35]. The longer blood circulation time for smaller MNPs such as ultrasmall superparamagnetic iron oxide (USPIO) nanoparticles had been well established in the literatures [52,53]. Our study suggests that the blood pool property of small MNPs could be observed *in vivo* since their first-passage, as early as the first few minutes through an organ system, as the delayed washout and elongated rMTT of the 50 nm MNPs.

Overall, PEGylation has effects on TTP, T50, and rMTT with shortening of the time intervals. This finding seems to indicate that PEGylation of MNPs may facilitate their passing through renal vasculature. More interestingly, the interaction shows a size difference in the PEGylation-related effects. Specifically, the effect of PEGylation-related

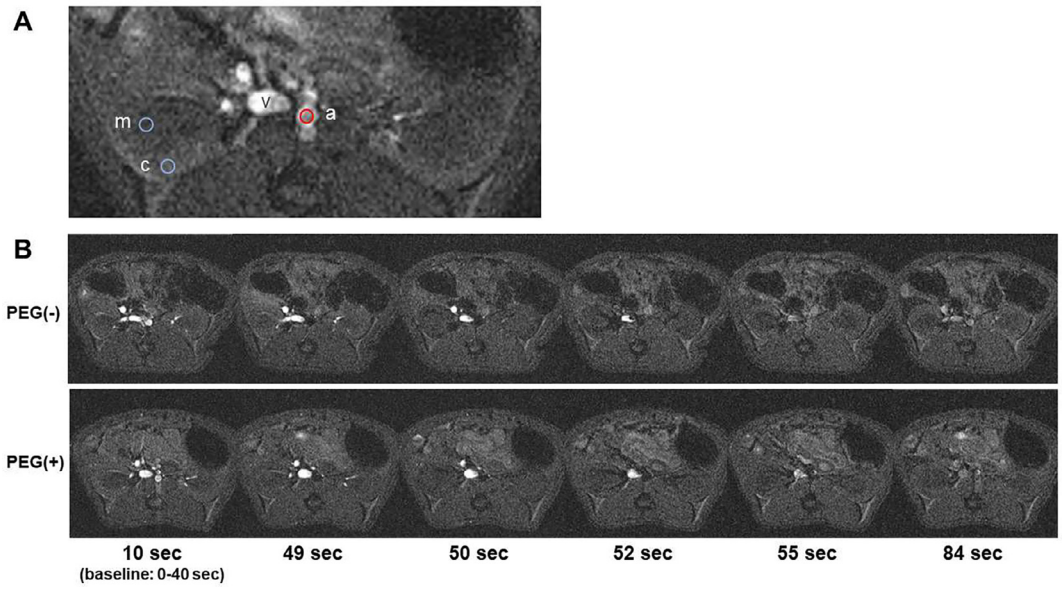

Fig. 1. (A) Anatomical location of rat kidneys with representative ROIs on aorta (a), renal cortex (c), and renal medulla (m), with respect to the location of inferior vena cava (IVC; v). (B) DSC perfusion MRI images of rat kidneys after bolus injection of 250 nm PEG(−) MNPs and PEG(+) MNPs. Note the dynamic changes in signal intensity represent MNPs passing through the kidneys: a transient drop in signal intensity first occurs in abdominal aorta at the 49-s images, then in renal large arteries and parenchyma at the 50-s and 52-s images, followed by gradual hypointense signals in IVC at the 52-s and 55-s images, and a partial recover of signal intensity in the large vessels at the 84-s images.

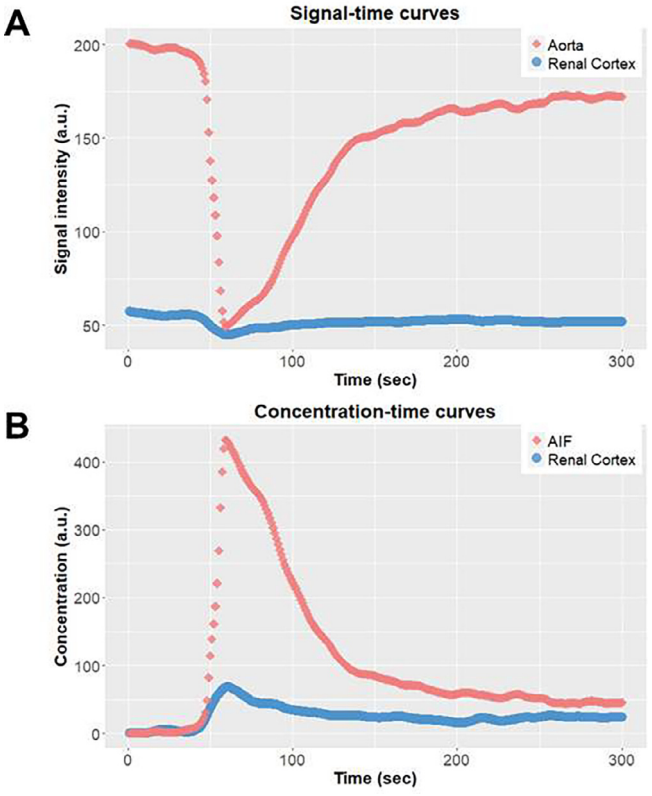

Fig. 2. Representative data postprocessing of perfusion MRI. (A) Signal-time curves (STCs) are derived from aorta and renal cortex ROIs after injection of 250 nm PEG(+) MNPs. (B) Concentration-time curves (CTCs) are converted from the respect STCs. The CTC of aorta is known as arterial input function (AIF).

facilitated passage is different for small- and large-sized MNPs. For 50 nm MNPs, the effect is significant, whereas for 250 nm MNPs, the effect of PEGylation seems to be overwhelmed by the size effect, becoming insignificant. This study indicates that surface coating material can affect the passage of MNPs through microcirculation, a process that can be observed by DSC perfusion MRI. Moreover, the importance of surface coating material on microcirculation increases as the particle size of MNPs decreases. To evaluate the effects of MNPs with different surface coating materials on microcirculation, DSC perfusion MRI may be a feasible method, especially for small-sized MNPs.

As for the evaluation of hemodynamic parameters, neither size nor PEGylation of MNPs makes a difference in the prediction of rRBF and rRBV with the same dosing concentration (5 mg/kg in our study). Therefore, correlation of rRBF and rRBV data derived from different size or coating materials of MNPs might be feasible in the future MR perfusion studies.

There were a few limitations of this study. First, the theoretical assumption for transformation of signal intensity-tracer concentration was based on linear relationship. However, in reality the relationship between ΔR2 and MNP concentration may not be linear. Factors such as water diffusion status could affect the transverse relaxation rate [19], therefore, more sophisticated modeling may be considered to analyze MR perfusion data. Second, there were artifacts related to bowel gas movement on the ventral portion of the kidneys that needed to be avoided with cautious while using a ROI approach. A pixel-by-pixel analysis may be considered in the future to exclude the pixels with extra noise.

For the future works, the combination of DSC MRI with MNPs as contrast agent may be useful in real-time evaluation of hemodynamic properties of different MNPs, surveying microcirculation properties of different organs, assessing tumors and vascular abnormalities of variable renal pathologies, and may have a role in detection of acute renal transplant rejection.

5. Conclusion

In summary, this work demonstrates the feasibility for DSC MRI to study the dynamic process of MNPs in the circulation. Effects of particle size and PEGylation of MNPs on organ microcirculation can be evaluated with perfusion MRI in rats. Particle size of MNPs dominates their kinetic process in the bloodstream, with small-sized MNPs showing

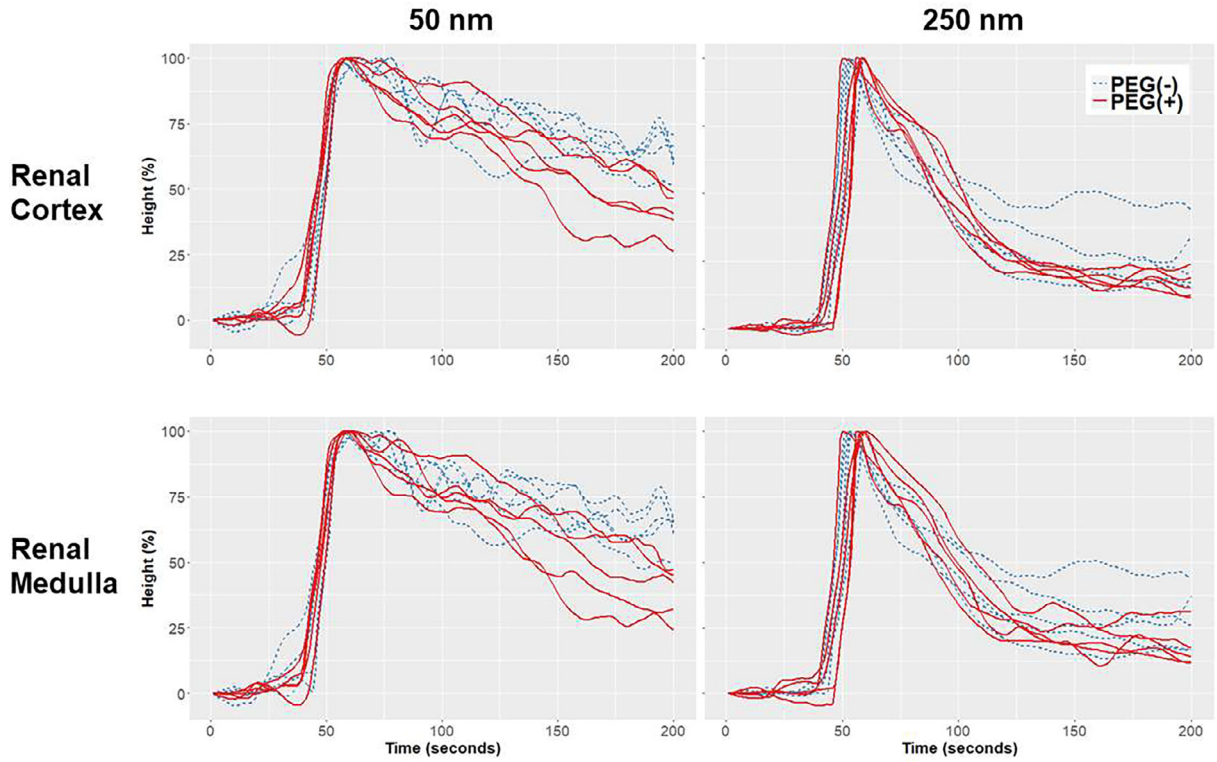

Fig. 3. Effects of PEGylation and particle size of MNPs on tissue impulse response functions (IRFs) of rat kidneys. IRFs are derived from deconvolution of CTCs of renal cortex and medulla from the AIF. Each tracing is derived from result of one rat. The characteristics of IRFs from different particles are evaluated with quantitative analysis in Fig. 4.

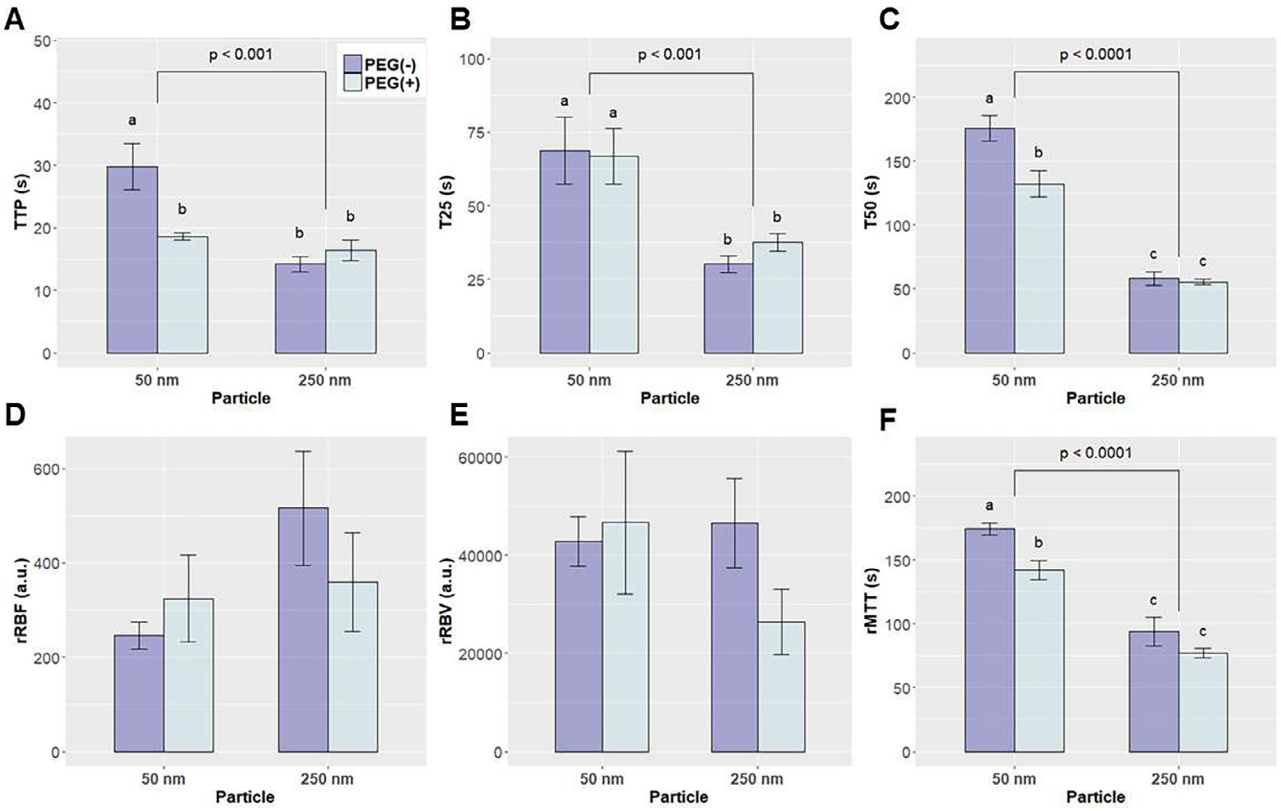

Fig. 4. Effects of PEGylation and particle size of MNPs on perfusion parameters of renal cortex of rats. Comparisons with statistical differences ($p < 0.05$) analyzed by ANOVA and post hoc Duncan tests are labeled with *p*-values and different alphabet letters (a, b, c), respectively. Values are presented as means ± SEM (n = 5).

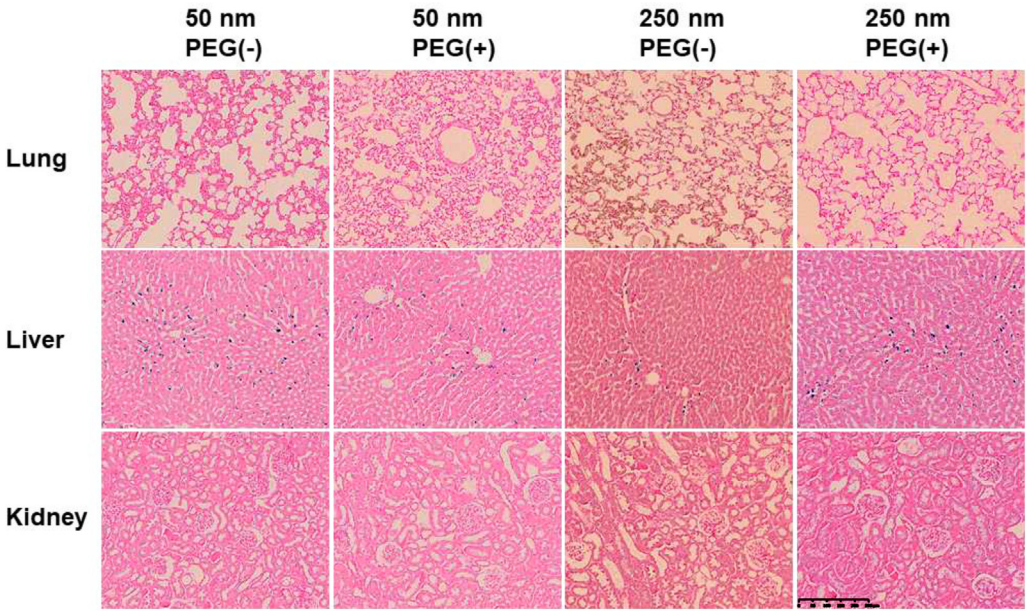

Fig. 5. MNP distribution in the liver, but not the kidney or lung of the rats. The results are representative Prussian blue-stained histological sections of 2–4 rats in each group.

slower wash in, delayed washout, and longer retention in the kidneys. Effect of PEGylation of MNPs depends on particle size, becoming significant as the particle size decreases, presenting with shortened T50 and rMTT in the 50 nm MNPs. Neither particle size, PEGylation, or their interaction influences on the prediction of rRBF and rRBV, therefore, hemodynamic parameters might be correlated in the future work of perfusion MRI using MNPs.

Acknowledgements

We thank the assistance of Shao-Chieh Chiu and the Center for Advanced Molecular Imaging and Translation, Chang Gung Memorial Hospital, Linkou, Taiwan. This work was supported by funding from Chang Gung Memorial Hospital (CMRPD1E0013, BMRP432 and CIRPG3D0161-3).

Appendix A. Supplementary data

Supplementary data to this article can be found online at https://doi.org/10.1016/j.jmmm.2018.11.041.

References

[1] S. Laurent, D. Forge, M. Port, A. Roch, C. Robic, L. Vander Elst, R.N. Muller, Magnetic iron oxide nanoparticles: synthesis, stabilization, vectorization, physicochemical characterizations, and biological applications, Chem. Rev. 108 (2008) 2064–2110.
[2] Q.A. Pankhurst, J. Connolly, S.K. Jones, J. Dobson, Applications of magnetic nanoparticles in biomedicine, J. Phys. D Appl. Phys. 36 (2003) R167.
[3] O.L. Gobbo, K. Sjaastad, M.W. Radomski, Y. Volkov, A. Prina-Mello, Magnetic nanoparticles in cancer theranostics, Theranostics 5 (2015) 1249–1263.
[4] D. Chang, M. Lim, J.A.C.M. Goos, R. Qiao, Y.Y. Ng, F.M. Mansfeld, M. Jackson, T.P. Davis, M. Kavallaris, Biologically targeted magnetic hyperthermia: potential and limitations, Front. Pharmacol. 9 (2018) 831.
[5] J.E. Rosen, L. Chan, D.B. Shieh, F.X. Gu, Iron oxide nanoparticles for targeted cancer imaging and diagnostics, Nanomedicine 8 (2012) 275–290.
[6] S. Boutry, S. Laurent, L.V. Elst, R.N. Muller, Specific E-selectin targeting with a superparamagnetic MRI contrast agent, Contrast Media Mol. Imaging 1 (2006) 15–22.
[7] M.A. Abakumov, N.V. Nukolova, M. Sokolsky-Papkov, S.A. Shein, T.O. Sandalova, H.M. Vishwasrao, N.F. Grinenko, I.L. Gubsky, A.M. Abakumov, A.V. Kabanov, V.P. Chekhonin, VEGF-targeted magnetic nanoparticles for MRI visualization of brain tumor, Nanomedicine 11 (2015) 825–833.
[8] B.W. Tse, G.J. Cowin, C. Soekmadji, L. Jovanovic, R.S. Vasireddy, M.T. Ling, A. Khatri, T. Liu, B. Thierry, P.J. Russell, PSMA-targeting iron oxide magnetic nanoparticles enhance MRI of preclinical prostate cancer, Nanomedicine (Lond) 10 (2015) 375–386.
[9] L. Deng, X. Ke, Z. He, D. Yang, H. Gong, Y. Zhang, X. Jing, J. Yao, J. Chen, A MSLN-targeted multifunctional nanoimmunoliposome for MRI and targeting therapy in pancreatic cancer, Int. J. Nanomed. 7 (2012) 5053–5065.
[10] T. Suwa, S. Ozawa, M. Ueda, N. Ando, M. Kitajima, Magnetic resonance imaging of esophageal squamous cell carcinoma using magnetite particles coated with anti-epidermal growth factor receptor antibody, Int. J. Cancer 75 (1998) 626–634.
[11] D. Artemov, N. Mori, B. Okollie, Z.M. Bhujwalla, MR molecular imaging of the Her-2/neu receptor in breast cancer cells using targeted iron oxide nanoparticles, Magn. Reson. Med. 49 (2003) 403–408.
[12] R. Singh, J.W. Lillard, Nanoparticle-based targeted drug delivery, Exp. Mol. Pathol. 86 (2009) 215–223.
[13] A.Z. Wilczewska, K. Niemirowicz, K.H. Markiewicz, H. Car, Nanoparticles as drug delivery systems, Pharmacol. Rep. 64 (2012) 1020–1037.
[14] V. Mulens, M. del Puerto Morales, D.F. Barber, Development of magnetic nanoparticles for cancer gene therapy: a comprehensive review, ISRN Nanomater. 2013 (2013) 14.
[15] J. Chomoucka, J. Drbohlavova, D. Huska, V. Adam, R. Kizek, J. Hubalek, Magnetic nanoparticles and targeted drug delivering, Pharmacol. Res. 62 (2010) 144–149.
[16] M. Shen, F. Gong, P. Pang, K. Zhu, X. Meng, C. Wu, J. Wang, H. Shan, X. Shuai, An MRI-visible non-viral vector for targeted Bcl-2 siRNA delivery to neuroblastoma, Int. J. Nanomed. 7 (2012) 3319–3332.
[17] E.X. Wu, H. Tang, J.H. Jensen, Applications of ultrasmall superparamagnetic iron oxide contrast agents in the MR study of animal models, NMR Biomed. 17 (2004) 478–483.
[18] J.L. Boxerman, L.M. Hamberg, B.R. Rosen, R.M. Weisskoff, MR contrast due to intravascular magnetic susceptibility perturbations, Magn. Reson. Med. 34 (1995) 555–566.
[19] R.P. Kennan, J. Zhong, J.C. Gore, Intravascular susceptibility contrast mechanisms in tissues, Magn. Reson. Med. 31 (1994) 9–21.
[20] C. Boyer, M.R. Whittaker, V. Bulmus, J. Liu, T.P. Davis, The design and utility of polymer-stabilized iron-oxide nanoparticles for nanomedicine applications, NPG Asia Mater. 2 (2010) 23.
[21] E. Illés, M. Szekeres, E. Kupcsik, I.Y. Tóth, K. Farkas, A. Jedlovszky-Hajdú, E. Tombácz, PEGylation of surfacted magnetite core–shell nanoparticles for biomedical application, Colloids Surf. A 460 (2014) 429–440.
[22] J.V. Jokerst, T. Lobovkina, R.N. Zare, S.S. Gambhir, Nanoparticle PEGylation for imaging and therapy, Nanomedicine (Lond) 6 (2011) 715–728.
[23] A.J. Cole, A.E. David, J. Wang, C.J. Galban, H.L. Hill, V.C. Yang, Polyethylene glycol modified, cross-linked starch-coated iron oxide nanoparticles for enhanced magnetic tumor targeting, Biomaterials 32 (2011) 2183–2193.
[24] D.P. Cormode, G.O. Skajaa, A. Delshad, N. Parker, P.A. Jarzyna, C. Calcagno, M.W. Galper, T. Skajaa, K.C. Briley-Saebo, H.M. Bell, R.E. Gordon, Z.A. Fayad, S.L. Woo, W.J. Mulder, A versatile and tunable coating strategy allows control of nanocrystal delivery to cell types in the liver, Bioconjug. Chem. 22 (2011) 353–361.
[25] J.R. Petrella, J.M. Provenzale, MR perfusion imaging of the brain: techniques and applications, AJR Am. J. Roentgenol. 175 (2000) 207–219.
[26] H.J. Michaely, S.O. Schoenberg, N. Oesingmann, C. Ittrich, C. Buhlig, D. Friedrich, A. Struwe, J. Rieger, C. Reininger, W. Samtleben, M. Weiss, M.F. Reiser, Renal artery stenosis: functional assessment with dynamic MR perfusion measurements–feasibility study, Radiology 238 (2006) 586–596.

[27] M. Notohamiprodjo, M.F. Reiser, S.P. Sourbron, Diffusion and perfusion of the kidney, Eur. J. Radiol. 76 (2010) 337–347.
[28] M.A. Rosen, M.D. Schnall, Dynamic contrast-enhanced magnetic resonance imaging for assessing tumor vascularity and vascular effects of targeted therapies in renal cell carcinoma, Clin. Cancer Res. 13 (2007) 770s–776s.
[29] N. Grenier, F. Cornelis, Y. Le Bras, G. Rigou, J.R. Boutault, M. Bouzgarrou, Perfusion imaging in renal diseases, Diagn. Interv. Imaging 94 (2013) 1313–1322.
[30] L.J. Wang, Key Diagnostic Features in Uroradiology: A Case-Based Guide, first ed., Springer International Publishing, 2015.
[31] S.O. Schoenberg, S. Aumann, A. Just, M. Bock, M.V. Knopp, L.O. Johansson, H. Ahlstrom, Quantification of renal perfusion abnormalities using an intravascular contrast agent (part 2): results in animals and humans with renal artery stenosis, Magn. Reson. Med. 49 (2003) 288–298.
[32] D. Yang, Q. Ye, M. Williams, Y. Sun, T.C. Hu, D.S. Williams, J.M. Moura, C. Ho, USPIO-enhanced dynamic MRI: evaluation of normal and transplanted rat kidneys, Magn. Reson. Med. 46 (2001) 1152–1163.
[33] C. Ronco, F. Stacul, P.A. McCullough, Subclinical acute kidney injury (AKI) due to iodine-based contrast media, Eur. Radiol. 23 (2013) 319–323.
[34] E.A. Sadowski, L.K. Bennett, M.R. Chan, A.L. Wentland, A.L. Garrett, R.W. Garrett, A. Djamali, Nephrogenic systemic fibrosis: risk factors and incidence estimation, Radiology 243 (2007) 148–157.
[35] H. Arami, A. Khandhar, D. Liggitt, K.M. Krishnan, In vivo delivery, pharmacokinetics, biodistribution and toxicity of iron oxide nanoparticles, Chem Soc Rev 44 (2015) 8576–8607.
[36] C.Z. Simonsen, L. Ostergaard, P. Vestergaard-Poulsen, L. Rohl, A. Bjornerud, C. Gyldensted, CBF and CBV measurements by USPIO bolus tracking: reproducibility and comparison with Gd-based values, J. Magn. Reson. Imaging 9 (1999) 342–347.
[37] M.R. Bashir, L. Bhatti, D. Marin, R.C. Nelson, Emerging applications for ferumoxytol as a contrast agent in MRI, J. Magn. Reson. Imaging 41 (2015) 884–898.
[38] E.A. Neuwelt, B.E. Hamilton, C.G. Varallyay, W.R. Rooney, R.D. Edelman, P.M. Jacobs, S.G. Watnick, Ultrasmall superparamagnetic iron oxides (USPIOs): a future alternative magnetic resonance (MR) contrast agent for patients at risk for nephrogenic systemic fibrosis (NSF)? Kidney Int. 75 (2009) 465–474.
[39] S. Mukundan, M.L. Steigner, L.L. Hsiao, S.K. Malek, S.G. Tullius, M.S. Chin, A.M. Siedlecki, Ferumoxytol-enhanced magnetic resonance imaging in late-stage CKD, Am. J. Kidney Dis. 67 (2016) 984–988.
[40] R. Bachmann, R. Conrad, B. Kreft, O. Luzar, W. Block, S. Flacke, D. Pauleit, F. Traber, J. Gieseke, K. Saebo, H. Schild, Evaluation of a new ultrasmall superparamagnetic iron oxide contrast agent Clariscan, (NC100150) for MRI of renal perfusion: experimental study in an animal model, J. Magn. Reson. Imaging 16 (2002) 190–195.
[41] S. Aumann, S.O. Schoenberg, A. Just, K. Briley-Saebo, A. Bjornerud, M. Bock, G. Brix, Quantification of renal perfusion using an intravascular contrast agent (part 1): results in a canine model, Magn. Reson. Med. 49 (2003) 276–287.
[42] R Core Team, R: A Language and Environment for Statistical Computing, R Foundation for Statistical Computing, Vienna, Austria, 2016.
[43] M. Dujardin, S. Sourbron, R. Luypaert, D. Verbeelen, T. Stadnik, Quantification of renal perfusion and function on a voxel-by-voxel basis: a feasibility study, Magn. Reson. Med. 54 (2005) 841–849.
[44] V.G. Kiselev, On the theoretical basis of perfusion measurements by dynamic susceptibility contrast MRI, Magn. Reson. Med. 46 (2001) 1113–1122.
[45] G.H. Jahng, K.L. Li, L. Ostergaard, F. Calamante, Perfusion magnetic resonance imaging: a comprehensive update on principles and techniques, Korean J. Radiol. 15 (2014) 554–577.
[46] L. Østergaard, R.M. Weisskoff, D.A. Chesler, C. Gyldensted, B.R. Rosen, High resolution measurement of cerebral blood flow using intravascular tracer bolus passages. Part I: mathematical approach and statistical analysis, Magn. Reson. Med. 36 (1996) 715–725.
[47] L. Ostergaard, A.G. Sorensen, K.K. Kwong, R.M. Weisskoff, C. Gyldensted, B.R. Rosen, High resolution measurement of cerebral blood flow using intravascular tracer bolus passages. Part II: experimental comparison and preliminary results, Magn. Reson. Med. 36 (1996) 726–736.
[48] P. Meier, K.L. Zierler, On the theory of the indicator-dilution method for measurement of blood flow and volume, J. Appl. Physiol. 6 (1954) 731–744.
[49] L. Kaufman, D.M. Kramer, L.E. Crooks, D.A. Ortendahl, Measuring signal-to-noise ratios in MR imaging, Radiology 173 (1989) 265–267.
[50] M.J. Firbank, A. Coulthard, R.M. Harrison, E.D. Williams, A comparison of two methods for measuring the signal to noise ratio on MR images, Phys. Med. Biol. 44 (1999) N261–264.
[51] J.E. Zuckerman, C.H.J. Choi, H. Han, M.E. Davis, Polycation-siRNA nanoparticles can disassemble at the kidney glomerular basement membrane, Proc. Natl. Acad. Sci. U.S.A 109 (2012) 3137–3142.
[52] R. Weissleder, A. Bogdanov, E.A. Neuwelt, M. Papisov, Long-circulating iron oxides for MR imaging, Adv. Drug Deliv. Rev. 16 (1995) 321–334.
[53] K.C. Briley-Saebo, Y.S. Cho, P.X. Shaw, S.K. Ryu, V. Mani, S. Dickson, E. Izadmehr, S. Green, Z.A. Fayad, S. Tsimikas, Targeted iron oxide particles for in vivo magnetic resonance detection of atherosclerotic lesions with antibodies directed to oxidation-specific epitopes, J. Am. Coll. Cardiol. 57 (2011) 337–347.